The 2D Analytic Signal for Envelope Detection and Feature Extraction on Ultrasound Images

Christian Wachinger*, Tassilo Klein, Nassir Navab

Computer Aided Medical Procedures (CAMP), Technische Universität München, München, Germany

Abstract

The fundamental property of the analytic signal is the split of identity, meaning the separation of qualitative and quantitative information in form of the local phase and the local amplitude, respectively. Especially the structural representation, independent of brightness and contrast, of the local phase is interesting for numerous image processing tasks. Recently, the extension of the analytic signal from 1D to 2D, covering also intrinsic 2D structures, was proposed. We show the advantages of this improved concept on ultrasound RF and B-mode images. Precisely, we use the 2D analytic signal for the envelope detection of RF data. This leads to advantages for the extraction of the information-bearing signal from the modulated carrier wave. We illustrate this, first, by visual assessment of the images, and second, by performing goodness-of-fit tests to a Nakagami distribution, indicating a clear improvement of statistical properties. The evaluation is performed for multiple window sizes and parameter estimation techniques. Finally, we show that the 2D analytic signal allows for an improved estimation of local features on B-mode images.

Keywords: Ultrasound, Demodulation, RF, Analytic Signal

1. Introduction

The analytic signal (AS) enables to extract local, low-level features from images. It has the fundamental property of split of identity, meaning that it separates qualitative and quantitative information of a signal in form of the *local phase* and the *local amplitude*, respectively. These quantities further fulfill invariance and equivariance properties (Felsberg and Sommer, 2001), allowing for an extraction of structural information that is invariant to brightness or contrast changes in the image. Exactly these properties lead to a multitude of applications in computer vision and medical imaging, such as registration (Carneiro and Jepson, 2002; Grau et al., Sept. 2007; Mellor and Brady, 2005; Zang et al., 2007; Zhang et al., 2007), detection (Estepar et al., 2006; Mulet-Parada and Noble, 2000; Szilágyi and Brady, 2009; Xiaoxun and Yunde, 2006), segmentation (Ali et al., 2008; Hacihaliloglu et al., 2008; Wang et al., 2009),

and stereo (Fleet et al., 1991). Phase-based processing is particularly interesting for ultrasound images because they are affected by significant brightness variations (Grau et al., Sept. 2007; Hacihaliloglu et al., 2008; Mellor and Brady, 2005; Mulet-Parada and Noble, 2000).

For 1D, the local phase is calculated with the 1D analytic signal. For 2D, several extensions of the analytic signal are proposed, with the *monogenic signal* (Felsberg and Sommer, 2001) presenting an isotropic extension. The description of the signal's structural information (phase and amplitude) is extended by a geometric component, the *local orientation*. The local orientation indicates the orientation of intrinsic 1D (i1D) structures in 2D images, see figure 1. This already points to the limitation of the monogenic signal; it is restricted to the subclass of i1D signals. Recently, Wietzke et al. (2009) proposed the *2D analytic signal*, which is an extension to the monogenic signal that permits the analysis of intrinsic two dimensional (i2D) signals. Therefore, the 2D signal analysis is embedded into 3D projective space and a new geometric quantity, the *apex angle*, is introduced. The 2D analytic signal also has the advantage of more accurately estimating local features from i1D signals (Wietzke et al., 2009).

*Corresponding Author. Present address: Massachusetts Institute of Technology, Cambridge, United States.

Email addresses: `wachinge@in.tum.de` (Christian Wachinger), `kleint@in.tum.de` (Tassilo Klein), `navab@in.tum.de` (Nassir Navab)

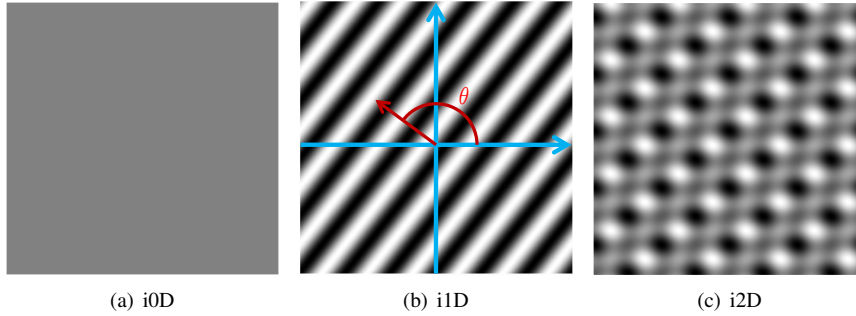|		
(a) i0D	(b) i1D	(c) i2D

Figure 1: Illustration of 2D signals with different intrinsic dimensionality. For i1D, we show the local orientation θ.

An initial version of this work was recently presented at a conference (Wachinger et al., 2011). The present article offers more detailed derivations, an improved statistical analysis, and more experimental results. In the remainder of this article, we show the advantages of the calculation of the 2D analytic signal for radio frequency (RF) and B-mode ultrasound images. Instead of performing the demodulation of RF signals for each scan line separately, we perform the demodulation in its 2D context with 2D Hilbert filters of first- and second-order. This leads to advantages in the envelope detection. Since all further processing steps of the creation of the B-mode image are based on the envelope, the improvement of the 2D envelope detection propagates to the quality of the B-mode image. Moreover, the result from the 2D envelope detection bears better statistical properties, as we illustrate with goodness-of-fit tests with a Nakagami distribution, with its implications to classification and segmentation. Finally, we show the advantages of the 2D analytic signal for estimating local features on B-mode images. All experiments are performed on clinical ultrasound images.

2. 2D Analytic Signal

There are various concepts to analyze the phase of signals, such as Fourier phase, instantaneous phase, and local phase (Granlund and Knutsson, 1995). We are primarily interested in the last two. For 1D signals, $g \in L^2(\mathbb{R})$, the instantaneous phase is defined as the argument of the analytic signal

$$\phi = \arg(g + i \cdot \mathcal{H}\{g\}), \qquad (1)$$

with $\mathcal{H}$ being the Hilbert transform and $i = \sqrt{-1}$. The instantaneous amplitude is the absolute value of the analytic signal

$$A = \sqrt{g^2 + \mathcal{H}\{g\}^2}. \qquad (2)$$

Since real signals consist of a superposition of multiple signals of different frequencies, the instantaneous phase, although local, can lead to wrong estimates. The signal has to be split up into multiple frequency bands, by means of bandpass filters, to achieve meaningful results, as further described in section 2.2.

Considering 2D signals, $f \in L^2(\mathbb{R}^2)$, the intrinsic dimension expresses the number of degrees of freedom to describe local structures (Zetsche and Barth, 1990). Intrinsic zero dimensional (i0D) signals are constant signals, i1D signals are lines and edges, and i2D are all other patterns in 2D, see figure 1. The monogenic signal is restricted to i1D signals and calculated with the two-dimensional Hilbert transform, also referred to as the Riesz transform. In the frequency domain, the first-order 2D Hilbert transform is obtained with the multiplication of

$$H_x^1(\mathbf{u}) = i \cdot \frac{x}{\|\mathbf{u}\|}, \qquad H_y^1(\mathbf{u}) = i \cdot \frac{y}{\|\mathbf{u}\|}, \qquad (3)$$

with $\mathbf{u} = (x, y) \in \mathbb{C}\backslash\{(0, 0)\}$.

For the calculation of the 2D analytic signal, higher order Hilbert transforms are used (Wietzke et al., 2009). The Fourier multipliers of the second-order Hilbert transform [1] are

$$H_{xx}^2(\mathbf{u}) = -\frac{x \cdot x}{\|\mathbf{u}\|^2}, \quad H_{xy}^2(\mathbf{u}) = -\frac{x \cdot y}{\|\mathbf{u}\|^2}, \quad H_{yy}^2(\mathbf{u}) = -\frac{y \cdot y}{\|\mathbf{u}\|^2}, \qquad (4)$$

again with $\mathbf{u} = (x, y) \in \mathbb{C}\backslash\{(0, 0)\}$. In contrast to Wietzke et al. (2009), we do not present the formulas of the Hilbert transforms in spatial but in frequency domain, which is more versatile for filtering, see section 2.2. Throughout the article we use upper case letters for filters and signals in frequency domain and lower case ones for their representation in spatial domain.

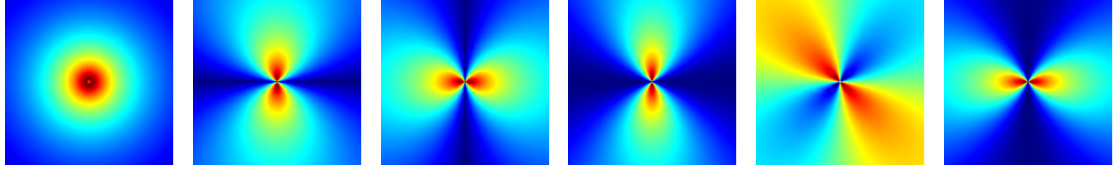[1]We want to thank the authors of (Wietzke et al., 2009) for discussions.

Figure 2: Magnitude of 2D Hilbert transforms with log-Gabor kernels in frequency domain. From left to right: B, $B \odot H_x^1$, $B \odot H_y^1$, $B \odot H_{xx}^2$, $B \odot H_{xy}^2$, $B \odot H_{yy}^2$.
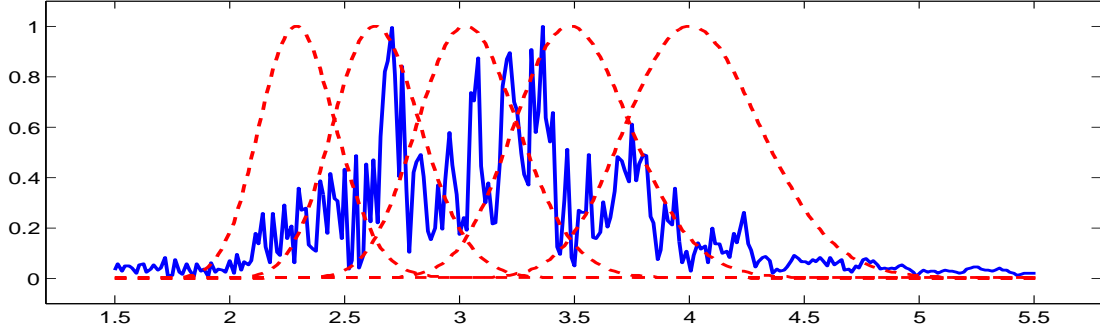

Figure 3: Log-Gabor filter bank consisting of 5 filters (red) and ultrasound signal spectrum (x-axis: frequency in MHz). Ultrasound acquisition frequency: 3.3 MHz.

2.1. Structural and Geometrical Features

The proposed extension of the 2D analytic signal is obtained by an embedding in 3D projective space. This allows for a differentiation of geometrical features (local orientation, local apex) and structural features (local phase, local amplitude). The filtered signal F_p, the first-order Hilbert transformed signals F_x, F_y, and the second-order Hilbert transformed signals F_{xx}, F_{xy}, F_{yy} are calculated with the bandpass filter B and the pointwise multiplication $\odot$ in frequency domain as

$$
\begin{bmatrix} F_p \\ F_x \\ F_y \end{bmatrix} = \begin{bmatrix} B \odot F \\ H_x^1 \odot B \odot F \\ H_y^1 \odot B \odot F \end{bmatrix} \tag{5}
$$

and

$$
\begin{bmatrix} F_{xx} \\ F_{xy} \\ F_{yy} \end{bmatrix} = \begin{bmatrix} H_{xx}^2 \odot B \odot F \\ H_{xy}^2 \odot B \odot F \\ H_{yy}^2 \odot B \odot F \end{bmatrix}. \tag{6}
$$

We illustrate the Hilbert transforms in frequency domain multiplied with log-Gabor bandpass filters in figure 2. In order to enable an interpretation of second-order Hilbert transformed signals in projective space, an isomorphism between the Hessian matrix and a vector valued representation is used (Wietzke et al., 2009), leading to $f_s = \frac{1}{2}[f_{xx} + f_{yy}]$, $f_+ = f_{xy}$, and $f_{+-} = \frac{1}{2}[f_{xx} - f_{yy}]$.

Finally, the local features are calculated as follows. The apex angle α, which differentiates between features of different intrinsic dimensionality, is

$$
\alpha = \arccos \frac{\sqrt{f_+^2 + f_{+-}^2}}{\|f_s\|}. \tag{7}
$$

With the apex angle, the homogeneous signal component f_h of the signal f_p in projective space is defined as

$$
f_h = \sqrt{\frac{1 + \cos \alpha}{2}}. \tag{8}
$$

The local orientation θ, local phase ϕ, and local amplitude A are calculated with

$$
\theta = \frac{1}{2} \arctan \frac{f_+}{f_{+-}}, \tag{9}
$$

$$
\phi = \text{atan2}\left(\sqrt{[f_h^{-1} f_x]^2 + [f_h^{-1} f_y]^2}, f_p \right), \tag{10}
$$

$$
A = \frac{1}{2} \sqrt{f_p^2 + [f_h^{-1} f_x]^2 + [f_h^{-1} f_y]^2}. \tag{11}
$$

For i1D signals, the homogeneous component is $f_h = 1$, and the formulas above reduce to the ones known from the monogenic signal.

2.2. Frequency Selection

Each signal f can be described with the Fourier series, decomposing the signal into components of dif-
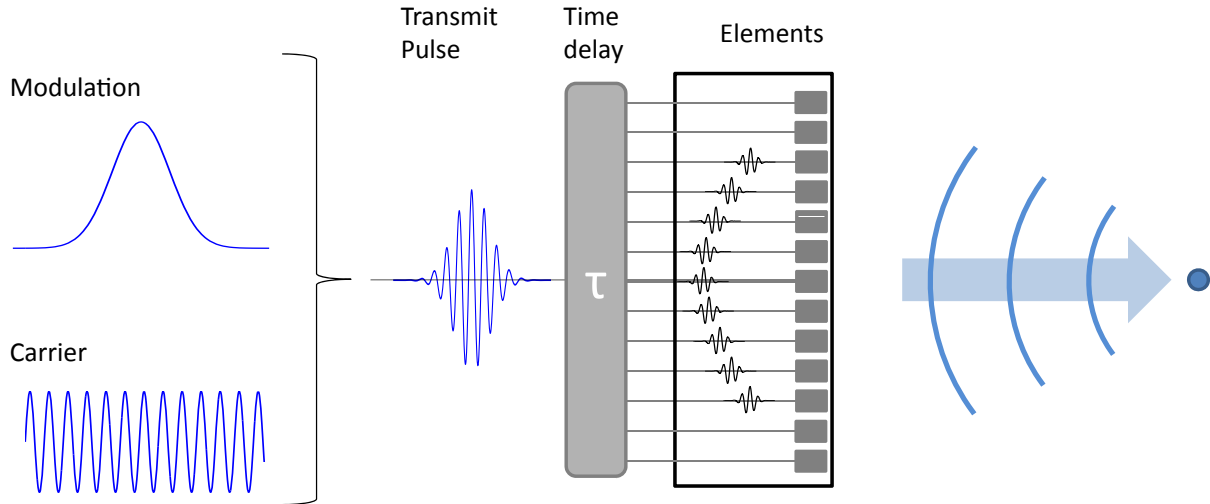
3

Figure 4: Transmission, from left to right. The combination of the modulation function and the carrier wave results in the transmit pulse. For focusing and beam steering, various time delays are added. The activation of the elements with the pulse pattern leads to the creation of a sound wave in the medium. The current center location is indicated as bold line.

ferent frequencies, each one having its own phase and amplitude. The direct application of the Hilbert transform on the original signal, which presents an accumulation of local signals from different frequencies, does therefore not adequately extract local features. Theoretically, we would need to calculate the analytic signal for infinitely narrow bandwidths, *i.e.*, Dirac deltas in the frequency domain. Following the uncertainty principle this results in filters with global support. Bandpass filters present an appropriate approximation for localization in spatial and frequency domain.

Felsberg and Sommer (2001) apply the difference of Poisson kernels for frequency selection. An interesting property of the Poisson filter is that it creates a linear scale-space (Felsberg and Sommer, 2004). Another filter that is commonly applied, especially in ultrasound, is the log-Gabor filter (Boukerroui et al., 2004; Grau et al., Sept. 2007; Hacihaliloglu et al., 2008; Mulet-Parada and Noble, 2000)

$$B(\mathbf{u}) = \exp\left(-\frac{\ln^2(\|\mathbf{u}\|/\gamma)}{2\ln^2(\kappa_\beta)}\right), \qquad (12)$$

with the center frequency γ and κ_β is related to the bandwidth β through $\kappa_\beta = \exp\left(-\frac{1}{4}\sqrt{2\ln(2)}\beta\right)$. Also in our analysis on ultrasound images, we achieve better results with the log-Gabor filter so that we concentrate on it in the following. A drawback of the log-Gabor filter is, however, that it has no analytic expression in the spatial domain. This is also the reason why we presented the

Hilbert transforms in equations (3) and (4) in frequency and not in spatial domain, as it is done in (Wietzke et al., 2009).

The design of a filter bank requires to balance the conflicting demands of uniform coverage of the spectrum and independence of each filter output. The important parameters are the filter bandwidth and the scaling factor between successive filters η. Starting from a base frequency γ_0, we calculate the center frequency γ_k of the k-th filter B_k with

$$\gamma_k = \gamma_0 \cdot \eta^k. \qquad (13)$$

In Kovesi (2008), a table of experimentally determined values for κ_β and η is presented that result in a minimal overlap of the filter transfer functions, while achieving an even spectral coverage. A filter bank with five log-Gabor filters is illustrated in figure 3. A study of alternative bandpass filters is presented by Boukerroui et al. (2004). For the further analysis, it is either possible to focus on the signal at one specific scale, or accumulate all responses from various scales, as it is *e.g.* done for the phase congruency (Kovesi, 1999). In our study, we also accumulate the responses from all filters B_k, as it is done for the calculation of phase congruency.

3. 2D Analytic Signal on RF Data

In the last section, we introduced the concepts of the 2D analytic signal. In this section, we apply these ad-
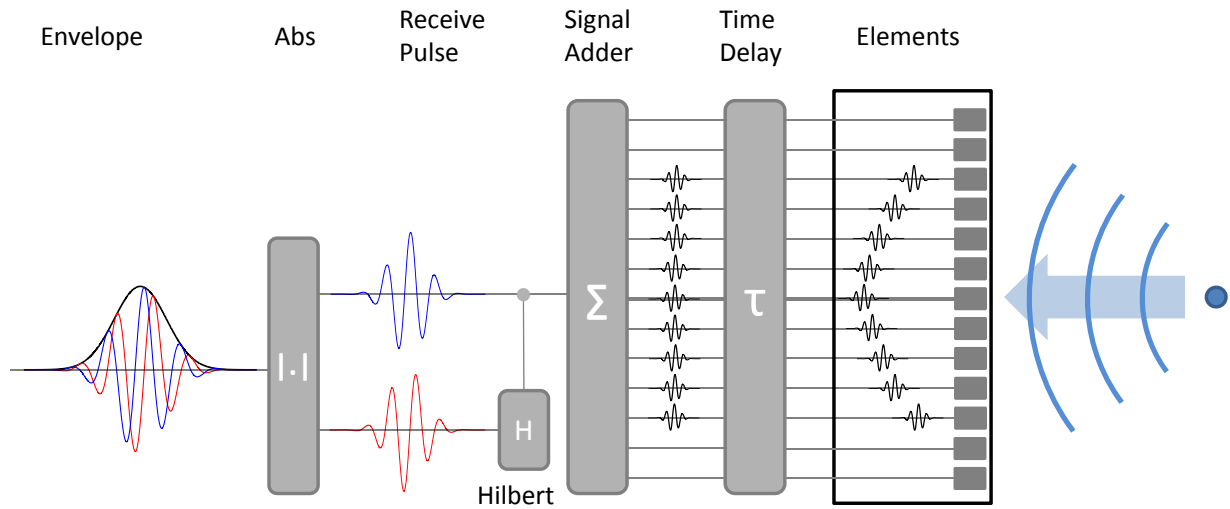
Figure 5: Reception, from right to left. The reflected sound waves in the medium are detected by the transducer elements. Each measured pulse is time delayed to compensate for differences in traveled distance. All received pulses are weighted and summed up to create the receive pulse (blue curve) for one location. The envelope (black curve) of the pulse is determined by calculating the absolute value of the analytic signal, consisting of the receive pulse and its Hilbert transform (red curve).

Figure 6: Exemplar ultrasound processing pipeline for RF to B-mode conversion.

vanced concepts for estimating the envelope of ultrasound RF data. Today's ultrasound probes are mainly transducer arrays, consisting of a group of closely arranged piezoelectric elements, where each element can be excited separately. This allows for electronic beam steering and focusing by delaying the firing of crystals. Further, a dynamic aperture can be created by flexibly activating a number of elements for transmission and reception. A schematic overview of ultrasound transmission and reception is shown in figures 4 and 5, respectively. The transmit pulse is created by convolving the modulation function with a carrier wave. In the example shown, we convolve a sinusoidal wave with a Gaussian modulator. Subsequently, a specific time delay is added to each element to account for focusing and steering. The created wavefront propagates in the medium and is reflected at inhomogeneities.

After the transmission, the elements are in receive mode and detect arriving waves, see figure 5. Since the traveled distance of the returning pulses is different for the various elements, delays have to be added to compensate for this. The delays change dynamically while echoes from deeper reflectors arrive. In the beam for-

mer, the echoes are amplified and accumulated with an additional weighting. This leads to the creation of a single receive signal for each position. Current transducers commonly operate with 128 elements, which leads in combination with slight beam steering to 256 different receive signals per image. The signal is subsequently passed through a pre-amplifier and a time gain compensation (TGC), which emphasizes signals from deeper regions to compensate for attenuation. The resulting signal is commonly referred to as radio-frequency (RF) signal and can be accessed in ultrasound systems.

3.1. RF to B-mode Conversion

For the creation of B-mode images, a sequence of processing steps is applied to the RF data (Hedrick et al., 2004; Zagzebski, 1996). Figure 6 illustrates the basic steps of the processing pipeline, including demodulation, non-linear intensity mapping, and filtering. The demodulation is one of the central parts and extracts the information-bearing signal from a modulated carrier wave. In ultrasound processing, the demodulation is commonly performed by an *envelope detection*. Hereby, the amplitude of the analytic signal is calculated for

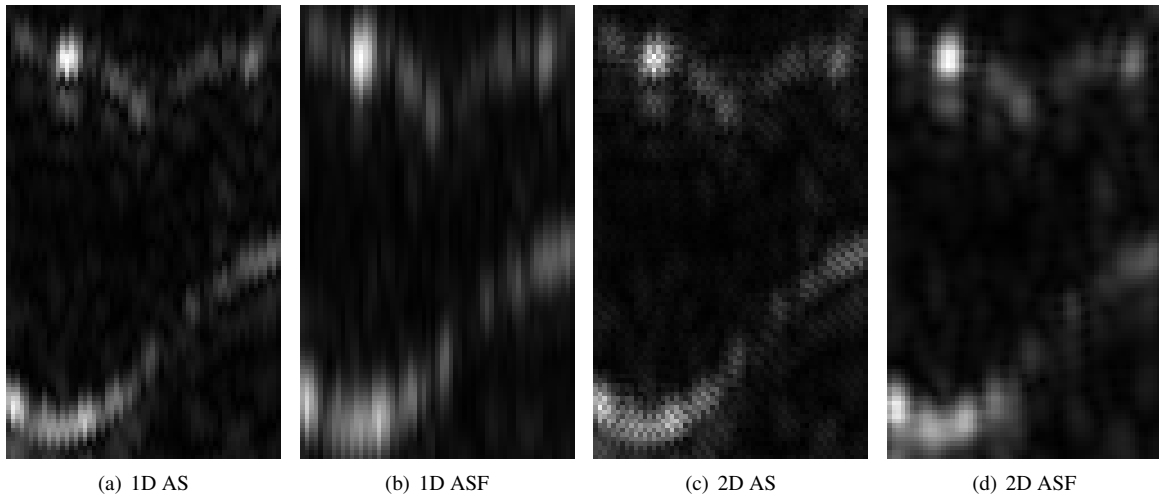| (a) 1D AS | (b) 1D ASF | (c) 2D AS | (d) 2D ASF |

Figure 7: Magnified region of envelope detected 2D image for various envelopes.

each of the 1D scan lines separately. Figure 5 illustrates the received signal (blue), the Hilbert transformed version (red), and the absolute value of the analytic signal (black), which is the envelope of the signal.

Interestingly, calculating the amplitude of the 1D analytic signal is equivalent to the *instantaneous amplitude*. In the literature of ultrasound imaging, it is noted that the quality of ultrasound images can be increased by multi-frequency decomposition and compounding of the received signal, simply referred to as *frequency compounding* (Cincotti et al., 2001). This is equivalent to the *local amplitude* estimation. This constitutes an interesting analogy, between the advantages of the frequency compounded signal to the normal one, on the one hand, and the advantage of the local amplitude in comparison to the instantaneous amplitude, on the other hand. We have neither seen this analogy noted in the literature before, nor the application of local amplitude and local phase techniques to RF data.

In contrast to the usually separate processing of each scan line, we consider all scan lines at once and construct the 2D analytic signal to estimate the local amplitude. This enables an improved envelope detection because the signal is analyzed in its 2D context by also considering information in lateral direction. The balance between influence from lateral and axial direction can be adjusted by the bandwidth in each direction of the bandpass filter, where the smaller spacing in axial direction should be considered accordingly. Note that we are not aware of any previous work that utilized any 2D extension of the analytic signal to perform the envelope detection in 2D.

3.2. Envelope and B-mode Results

We acquired 9 ultrasound RF datasets from different patients with an ultrasound system from Ultrasonix (Richmond, Canada) using a L14-5/38 linear transducer operated with a single focus region. Each dataset consists of three acquisitions. We experimented with three different acquisition frequencies, 3.3MHz, 6MHz, and 10MHz, and two different depth settings, 4cm and 6cm, in order to evaluate the universality of our method. The sampling frequency of the RF data is 40 MHz. We work with 5 filter scales, $k = 4$, with the bandwidth related $\kappa_\beta = 0.85$ and the corresponding multiplicative factor $\eta = 1.3$, as proposed in Kovesi (2008). We compare the envelope detection for: (i) 1D analytic signal (1D AS), (ii) 1D analytic signal with filter bank (1D ASF), (iii) monogenic signal (MS), and (iv) monogenic signal with filter bank (MSF), (v) 2D AS, and (vi) 2D ASF. Exemplarily, we show the frequency spectrum of one dataset acquired at 3.3Mhz together with the log-Gabor filter bank in figure 3. We present magnified regions of the various envelope images in figure 7. Note that we do not show the results of the MS, because the more interesting improvement is for 2D AS. However, we include them into the analysis of noise statistics in section 3.3. We can clearly observe that the 2D analytic signal leads to a more accurate and consistent extraction of structures. This becomes particularly clear on the circular structure on the top left, which appears rather ellipsoidal on the estimates from the 1D analytic signals. We also note the positive influence of the filter bank for the estimation of the 2D analytic signal.

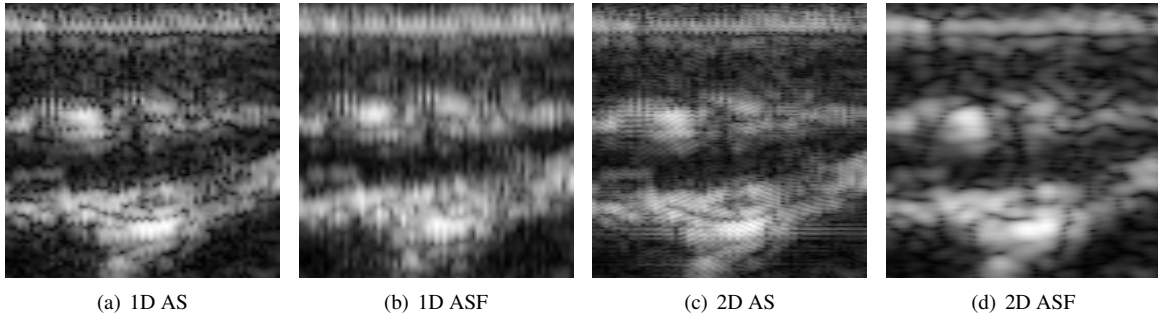Regarding the results of the envelope detection with

| | | | |
| (a) 1D AS | (b) 1D ASF | (c) 2D AS | (d) 2D ASF |

Figure 8: Magnified regions of images after log-compression.

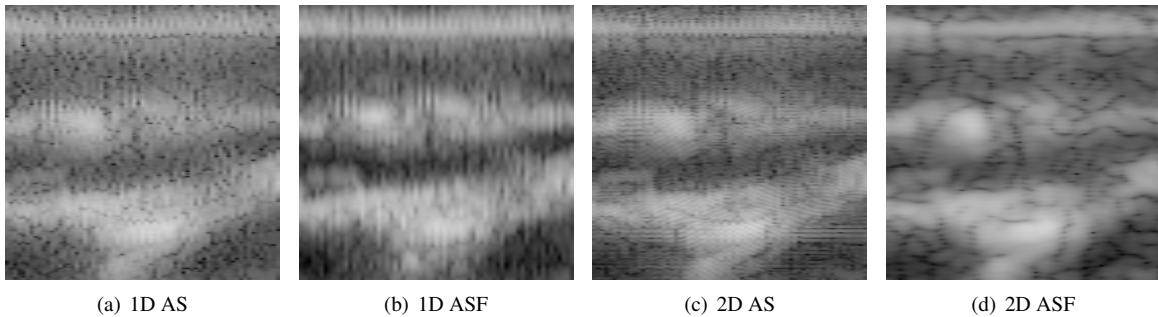| | | | |
| (a) 1D AS | (b) 1D ASF | (c) 2D AS | (d) 2D ASF |

Figure 9: Magnified regions of images after log-compression and MUCRO.

1D AS, we observe an artifact, where adjacent lines seem to be misaligned. This is due to standard double line density acquisitions, with every second line having steering applied. The artifact is not a result of the envelope detection but of the acquisition process, so inherently in the RF data. We observe that the artifact diminishes in combination with the filter bank, where especially the application of the 2D ASF leads to a significant reduction.

We perform an RF to B-mode conversion of local amplitude images A with a log-compression including a translation of 25, $\log(A + 25)$. The results for 1D ASF and 2D ASF on clinical data are shown in figure 8. The B-mode image resulting from the 2D analytic signal clearly shows more consistent structures and less noise. Typically, further filtering steps are applied to the log-compressed image to improve its visual appearance. These processing steps are proprietary to the manufacturer and generally not publicly accessible. Ultrasonix (Redmond, Canada), however, distributes a particular research system with a specific SDK including their post-processing filter, called MUCRO. We apply MUCRO to the log-compressed images, with the results shown in figure 9. Even after the application of

MUCRO, the advantages of the images from the 2D analytic signal are clearly visible. This is not self-evident because the post-processing methods are designed to be applied to 1D envelope detected images, still leaving room for improvement by adapting the post-processing to 2D envelope estimation. Finally, one of the reasons for applying the post-processing filtering is to establish consistency between scan lines, which we already achieve by the 2D envelope detection.

Next to clinical data, we also performed experiments on ultrasound images of a QA phantom from ATS laboratories (Bridgeport, CT, USA), Model 539 Multipurpose, which were acquired with the linear transducer at 6Mhz. The phantom contains monofilament line targets at different depths. The focus is set on the top one. Figure 10 shows magnifications of the results of various envelope detection techniques for the top line target. Although it is not clinical data, the phantom presents a more controlled environment, where we have a better understanding of the structures in the image. Scanning perpendicular to the line target, we expect a circular structure in the images. As previously, we observe an improvement by applying the 2D envelope detection, especially in combination with the filter bank.

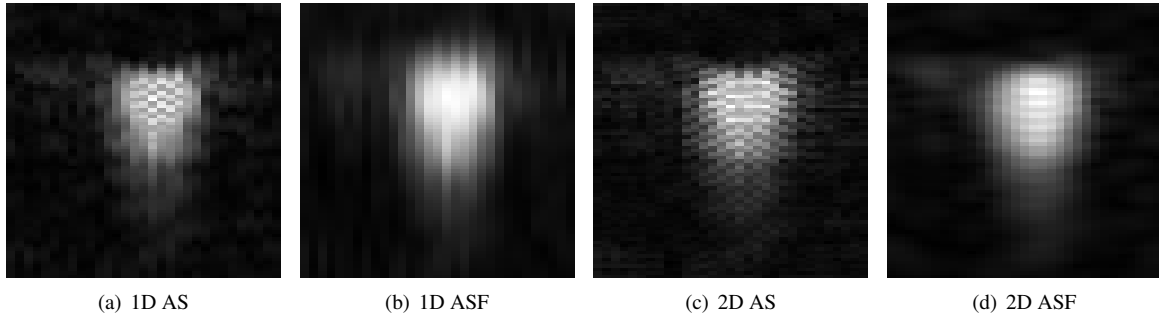| (a) 1D AS | (b) 1D ASF | (c) 2D AS | (d) 2D ASF |

Figure 10: Magnified region of envelope detected image for various techniques of line target of QA phantom.
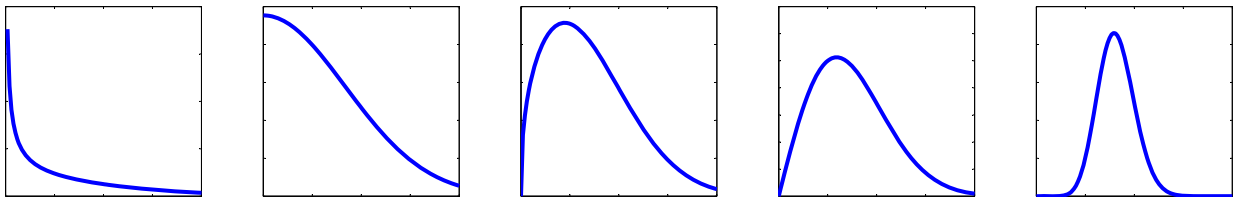

Figure 11: Plot of Nakagami distribution for various shape parameters m and fixed scaling parameter $\omega = 0.7$. From left to right: $0 < m < 0.5$ (pre-Rician), $m = 0.5$ (generalized Rician), $0.5 < m < 1$ (generalized Rician), $m = 1$ (Rayleigh), $m > 1$ (Rician).

3.3. Analysis of Envelope Statistics

Next to the visual assessment of the 2D envelope detection, we are interested in supporting the improvement by quantitative measurements. This is challenging because there does not exist a ground truth envelope signal that we could compare to our results. Note that also standard ultrasound simulation environments such as Field II (Jensen, 1999) only produce RF data. Interestingly, however, various noise distributions were derived from a theoretical analysis of speckle, which appears if the signal is composed of a multitude of independently phased additive complex components (Dutt, 1995; Goodman, 2006). The accumulation of all components creates a random walk. Each component is the result of a reflection of the pulse at a randomly located scatterer in the medium. In ultrasound, microscopic inhomogeneities due to the cellular nature of tissue are responsible for scattering (Cobbold, 2007).

Depending on the scattering scenario in the resolution cell, so on the number of scatterers and whether a coherent structure is existent, different statistical models have been proposed to model ultrasound data (Dutt, 1995). Among them there is Rayleigh (Kotropoulos et al., 1994), Rician (Shankar et al., 1993), pre-Rician K (Lord, 1954; Jakeman and Pusey, 1976), generalized K (Shankar, 1995), homodyned K (Dutt and Greenleaf, 1994), as well as Rician Inverse of the Gaus-

sian (Eltoft, 2003). Common to all these distributions is the inherent complexity, limiting its practical applicability. In order to address this issue, the Nakagami distribution (Nakagami, 1960) was proposed, because it admits an explicit analytical expression and it is versatile enough to model various scattering scenarios. Furthermore, it is used in a multitude of applications to model backscatter characteristics of US envelope data for segmentation and classification, see (Destrempes et al., 2009; Larrue and Noble, 2011; Shankar et al., 2002), as well as registration (Myronenko et al., 2009; Wachinger et al., 2012). In the following, we analyze the effects of the 2D envelope detection on the speckle statistics choosing the Nakagami model. In particular, we quantify the impact of the 2D analytic signal with goodness-of-fit tests. On the one hand, this allows to evaluate the correspondence between the theoretical speckle model and the calculated envelope. On the other hand, it indicates the advantage for the aforementioned applications - segmentation, classification, registration - which incorporate a statistical model based on the Nakagami distribution.

The Nakagami distribution with shape m and scale ω parameters is

$$p(x \mid m, \omega) = \frac{2m^m x^{2m-1}}{\Gamma(m)\omega^m} \exp\left(-\frac{m}{\omega}x^2\right), \forall x \in \mathbb{R}_+. \quad (14)$$
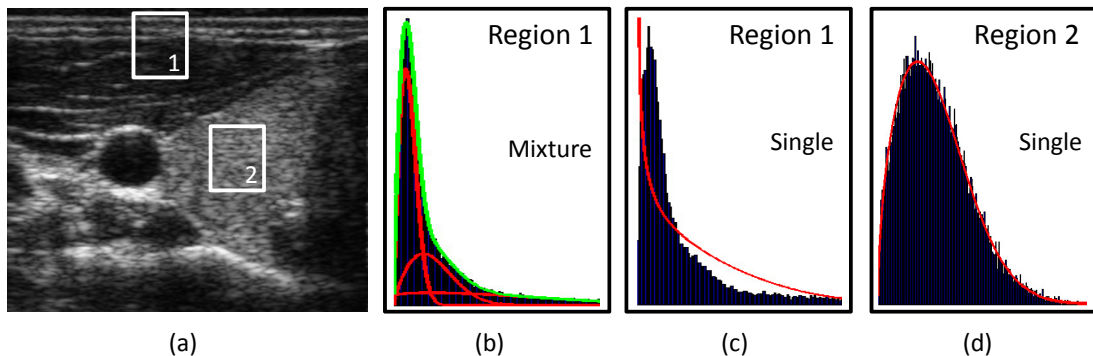
Figure 12: RF image with sample distributions estimated for two areas. Data in region 1 is mixture of Nakagami distributed and data of region 2 is single Nakagami distributed. Whereas MLE can fit nicely in region 2 (d) it expectedly performs poorly in region 1 (c), that can only be represented properly by a mixture (b).

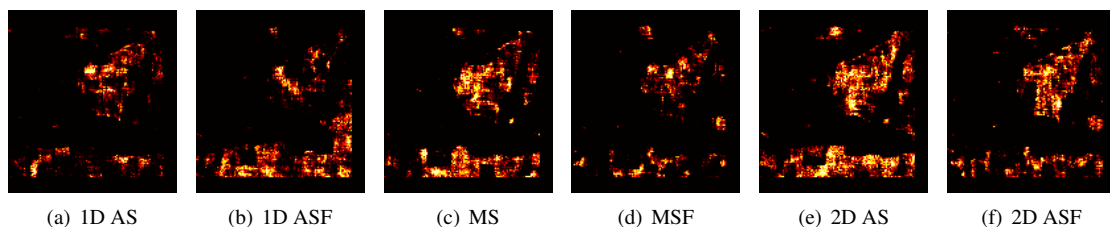(a) 1D AS   (b) 1D ASF   (c) MS   (d) MSF   (e) 2D AS   (f) 2D ASF

Figure 13: The P-values are calculated for all patches of an envelope image. Pixel brightness indicates P-value. We perform the calculation for various envelope detection techniques. Comparing the P-value images to the B-mode image in figure 12, we see that the bright regions correspond to homogeneous regions in the US image. The results shown correspond to patient 1, acquisition 1, and a large window size.

For $m = 1$, this corresponds to the Rayleigh distribution. For varying m, the Nakagami distribution can model pre- and post-Rayleigh as well as generalized Rician distributions (Shankar et al., 2001). Further, it is a good approximation to the homodyned K distribution (Destrempes and Cloutier, 2010). Figure 11 illustrates the Nakagami distribution for various shape parameters and fixed scale. Note that we only keep the scale fixed for illustrative purposes, while it is estimated together with the shape parameter during the fit.

3.3.1. Goodness-of-Fit Test

A goodness-of-fit (GOF) test evaluates if the data $d_1, \ldots, d_n$, under the assumption of i.i.d. samples, comes from the given theoretical probability distribution p (D'Agostino and Stephens, 1986). Note that conventional GOF tests are restricted to the case of single distributions. For inhomogeneous regions in the image, *e.g.* regions including tissue boundaries, a mixture of Nakagami is more appropriate. We illustrate this scenario in figure 12. Region 1 corresponds to an inhomogeneous region with reflections from the skin layers.

As seen in (b), a mixture of Nakagami achieves a perfect fit to the distribution of region 1, while the fit with a single distribution in (c) is not satisfying. For the homogeneous region 2, a fit with a single Nakagami distribution is sufficient, see (d). Consequently, we can only achieve good results with the GOF test on homogeneous image regions. The mixture case has to be further evaluated, with similar results to be expected.

For the GOF test, the range of the data is partitioned into M bins β_i, $i = 1, \ldots, M$, with N_i and the number of samples per bin. Moore suggests to divide the data into $M = 2n^{\frac{2}{5}}$ bins (D'Agostino and Stephens, 1986). Furthermore, we assume the bins to be equiprobable as suggested in (Bock and Krischer, 1998). In this regard, we let p_i be the integral of the distribution in the range β_i given the parameters of the distribution $\theta = \{m, \omega\}$

$$p_i = \int_{\beta_i} p(x \mid \theta) \, dx. \tag{15}$$

Hence, p_i expresses the likelihood of a sample to be in the bin β_i (identical for all bins). The test statistics underlying the GOF test is the sum of differences between
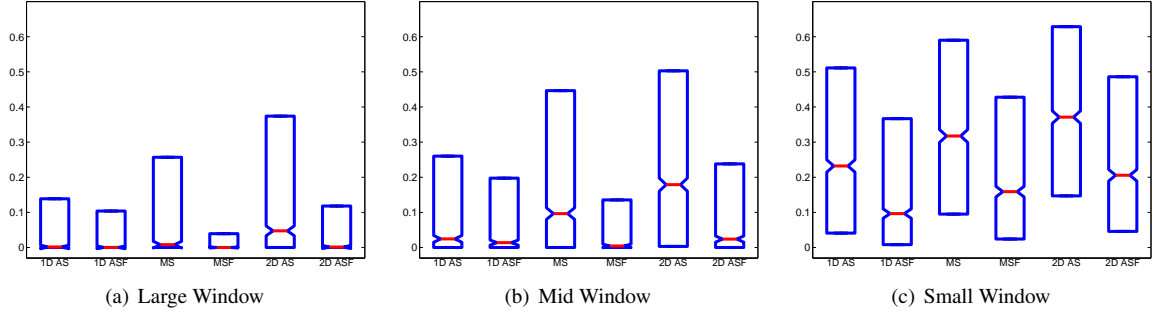
9

(a) Large Window   (b) Mid Window   (c) Small Window

Figure 14: Box plot of P-values for different envelope detections and window sizes for patient 1, acquisition 1.

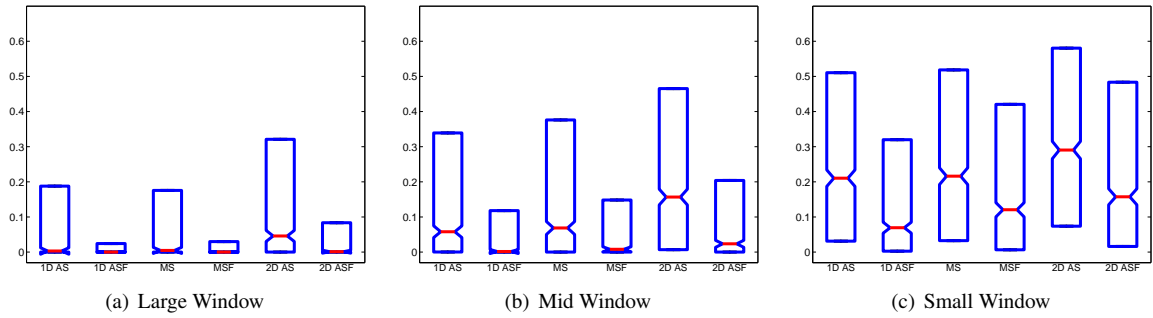(a) Large Window   (b) Mid Window   (c) Small Window

Figure 15: Box plot of P-values for different envelope detections and window sizes for patient 3, acquisition 3.

observed and expected outcome frequencies

$$X^2 = \sum_{i=1}^{M} \frac{(N_i - np_i)^2}{np_i}. \tag{16}$$

This yields a quadratic form in N_i that has approximately a χ distribution with $M - N - 1$ degrees of freedom and $N = 2$ the number of parameters of the distribution. In order to assess the GOF quantitatively, we employ the P-value based hypothesis test. The P-value serves as an indicator of how likely the null hypothesis H_0 is true. In our case, H_0 is the hypothesis that the observations are Nakagami distributed, leading to the following calculation of the P-value

$$P = \int_{X^2}^{\infty} \chi^2(M - N - 1)\, \mathrm{d}x, \tag{17}$$

employing equation (16) as the lower bound of integration.

3.3.2. Rao-Robson Statistic

Given the data, we first have to estimate the parameters m, ω of the Nakagami distribution before the GOF test is performed. This is, however, opposing the general assumption that the parameters of the distribution are a-priori given before the test is performed. Therefore, another quadratic form in N_i has to be used, with the Rao-Robson statistic being one possibility (D'Agostino and Stephens, 1986; Lin et al., 2005; Tao et al., 2006). Considering the parametric form of the distribution $p(x \mid \theta)$ and the maximum likelihood estimate $\hat{\theta}$, the Rao-Robson statistic is

$$RR = V^{\top}(\hat{\theta})Q(\hat{\theta})V(\hat{\theta}) \tag{18}$$

with

$$V(\theta) = \frac{N_i - np_i}{(np_i)^{1/2}} \tag{19}$$

$$Q(\theta) = I + D(\theta)[J(\theta) - D^{\top}(\theta)D(\theta)]^{-1}D^{\top}(\theta) \tag{20}$$

$$D_{ij}(\theta) = p_i(\theta)^{\frac{1}{2}}\frac{\partial p_i(\theta)}{\partial \theta_j}. \tag{21}$$

$J(\theta)$ is the $N \times N$ Fisher information matrix and I is an $M \times M$ identity matrix. The partial derivative with respect to the distribution parameters $\frac{\partial p_i(\theta)}{\partial \theta_j}$ is involved and presented in Appendix A. The Rao-Robson statistic is χ^2 distributed with $M - N - 1$ degrees of freedom, leading to P-values computed by

$$P = \int_{RR}^{\infty} \chi^2(M - N - 1)\, \mathrm{d}x \tag{22}$$

10

with the Rao-Robson statistic *RR* as lower bound of integration.

3.3.3. Distribution Parameter Estimation

An essential step before the Rao-Robson statistics can be calculated is the fitting of the Nakgami distribution to the data, resulting in the distribution parameters θ. One possibility for calculating the fit is to apply maximum likelihood estimation (MLE). However, as there is no closed-form solution this involves an iterative optimization procedure such as Newton's method. An alternative approach for calculating the parameters considers the 2nd and 4th moments

$$\omega = \mathrm{E}(x^2) \qquad (23)$$

and

$$m = \frac{[\mathrm{E}(x^2)]^2}{\mathrm{E}[x^2 - \mathrm{E}(x^2)]^2} \qquad (24)$$

with the latter being referred to as inverse normalized variance estimator (Abdi and Kaveh, 2000) and E the expected value.

The distribution parameters are estimated for local windows in the images. The size of the window is a tradeoff between sufficient statistics for the estimation and homogeneous structures in the patch. As detailed previously, a mixture fit is more appropriate for certain regions (see figure 12), whereas it is more likely to have homogeneous structures within smaller windows. Moreover, for applications such as tissue characterization and segmentation, the interest lies in working with small windows to achieve a high spatial resolution of the parameter map (Noble, 2010). The moment-based estimation depends on local histograms, which are not good approximations to the actual distribution for small windows, and further, the estimation of the parameters is unstable. The same holds for MLE. Larrue and Noble (2011) therefore propose the Gamma kernel density estimation (GKDE) for Nakagami imaging to achieve a good fit for a very limited number of data points. The usage of non-symmetric Gamma kernels

$$K_{x/b+1,b}(t) = \frac{t^{x/b} \cdot e^{-t/b}}{b^{x/b+1} \cdot \Gamma(x/b + 1)} \qquad (25)$$

was shown to lead to better results for the estimation of highly asymmetric distributions such as Nakagami or Gamma (Chen, 2000). The resulting Gamma kernel estimator for a window W containing the data $d_1, \ldots, d_l$ is

$$p(x) = \frac{1}{l} \sum_{j=1}^{l} K_{x/b+1,b}(d_j). \qquad (26)$$

The smoothness is controlled by the parameter b, behaving similarly to the variance in Gaussian-based density estimation. Larrue and Noble (2011) achieved good results by setting $b = 0.05$, which performed favorably in our experiments as well.

In our analysis, we work with three different window sizes, 80×10, 60×6, and 20×3, with more pixels being considered along the axial direction. For the two larger patch sizes, we achieve similar results for MLE and GKDE with moments, so that we work with the MLE estimates. For the smallest patch size, we use GKDE with moments because it leads to more robust estimates than MLE.

3.3.4. Statistical Results

We perform the statistical evaluation on all 9 datasets, each one consisting of 3 different acquisitions, resulting in 27 different images. Further, we use three different window sizes in order to evaluate the dependency on the window size. This leads to 81 different configurations for the estimation, where the Rao-Robson GOF test is performed densely throughout the image for all 6 types of envelope detections. By performing the test densely throughout the image, we can create a new image with the intensity values being the P-values. We show these images in figure 13 for the various envelope detection schemes for one configuration. The brighter the images, the higher the P-values, and consequently the better for statistical applications because we achieve better fits. We note that the bright regions are corresponding to the homogeneous areas in the ultrasound image because only these areas are appropriately modeled with a single distribution, as discussed previously.

Additionally, we calculate the statistics of the P-values. We show the box plot for four different configurations in figures 14 and 15. We refer the reader to the supplementary material for a complete list of box plots for all different configurations. The red line indicates the median and the box is constructed from the interquartile range. Our results therefore show that the envelope detection without the filter bank produces better fits, which makes sense, because the convolution with log-Gabor filters changes the distribution of the samples. More importantly, however, we note the improvement from 1D AS to MS, and further from MS to 2D AS. This shows on the one hand, the advantage of applying 2D Hilbert transforms in contrast to 1D ones, and on the other hand, the advantage of the 2D analytic signal in contrast to the monogenic signal. This confirms the visually improved results for 2D envelope detection from the previous section.

11

Table 1: The tables shows the percentage of P-Values above 0.85 for the various images and envelope detection schemes. The highest percentage across the envelope detection techniques is marked in bold.

Patient	Acqu	Frequency	Depth	Window	1D AS	1D ASF	MS	MSF	2D AS	2D ASF
1	1	3.3Mhz	4cm	Large	1.61	1.83	4.10	0.66	**4.76**	1.83
				Medium	2.77	2.38	5.04	1.83	**6.59**	2.60
				Small	5.70	3.32	6.98	4.60	**7.25**	4.49
1	2	3.3Mhz	4cm	Large	1.83	1.50	2.16	0.78	**4.71**	1.27
				Medium	2.60	1.77	4.60	1.38	**6.37**	2.60
				Small	4.60	3.38	6.48	4.37	**7.81**	5.76
1	3	3.3Mhz	4cm	Large	1.38	2.38	2.99	0.83	**4.37**	1.38
				Medium	2.60	1.77	4.60	1.38	**6.37**	2.60
				Small	4.76	2.38	6.92	4.26	**7.14**	4.49
2	1	6Mhz	5cm	Large	2.77	0.78	3.32	1.11	**4.32**	2.55
				Medium	3.10	1.11	4.43	1.66	**5.43**	2.21
				Small	**6.98**	4.32	5.43	4.76	5.32	5.54
2	2	6Mhz	5cm	Large	3.10	1.66	2.66	1.55	**3.88**	1.66
				Medium	3.43	1.00	4.54	1.55	**4.65**	3.21
				Small	6.31	3.65	3.99	4.87	**7.75**	4.43
2	3	6Mhz	5cm	Large	**4.21**	0.78	2.44	1.22	3.54	1.33
				Medium	2.88	1.77	3.77	2.88	**6.31**	3.10
				Small	4.98	3.54	4.65	5.43	**6.53**	5.98
3	1	10Mhz	4cm	Large	3.29	0.68	3.00	0.78	**3.59**	1.36
				Medium	5.04	1.55	4.65	0.58	**6.40**	1.94
				Small	3.29	3.39	5.52	3.88	**5.91**	3.68
3	2	10Mhz	4cm	Large	3.00	0.39	2.33	0.87	**3.39**	0.58
				Medium	3.59	1.84	3.88	1.74	**5.91**	1.16
				Small	6.30	2.81	4.46	3.59	**6.69**	3.88
3	3	10Mhz	4cm	Large	2.33	0.87	1.74	0.97	**3.29**	0.87
				Medium	3.78	1.16	4.26	2.03	**6.30**	2.52
				Small	4.17	2.91	5.04	4.17	**7.17**	3.78
4	1	6Mhz	5cm	Large	1.74	0.10	1.26	0.68	**1.94**	0.58
				Medium	2.62	0.78	2.62	1.36	**4.26**	1.65
				Small	3.88	3.00	4.46	4.65	**5.43**	4.26
4	2	6Mhz	5cm	Large	1.26	0.29	1.55	0.78	**3.00**	1.45
				Medium	2.81	1.74	2.91	2.13	**3.59**	1.84
				Small	4.26	3.10	5.23	3.59	**5.91**	3.10
4	3	6Mhz	5cm	Large	1.55	0.39	1.45	0.58	**2.62**	0.68
				Medium	2.52	0.48	4.07	1.55	**5.33**	1.65
				Small	4.94	2.62	4.55	4.84	4.65	**5.23**
5	1	10Mhz	4cm	Large	0.97	0.19	1.55	0.48	**2.23**	0.87
				Medium	2.23	1.16	1.94	1.26	**4.94**	1.65
				Small	4.46	2.23	4.65	3.49	**5.91**	3.59
5	2	10Mhz	4cm	Large	1.55	0.39	2.13	0.87	**2.23**	0.87
				Medium	2.03	0.87	2.33	0.29	**5.23**	1.55
				Small	5.04	3.59	**6.10**	4.55	4.07	3.68

Table 2: The tables shows the percentage of P-Values above 0.85 for the various images and envelope detection schemes. The highest percentage across the envelope detection techniques is marked in bold.

| Patient	Acqu	Frequency	Depth	Window	1D AS	1D ASF	MS	MSF	2D AS	2D ASF
5	3	10Mhz	4cm	Large	0.97	0.19	1.07	0.58	**2.42**	0.48
				Medium	2.62	0.97	3.00	1.07	**3.68**	1.36
				Small	3.88	2.23	4.07	3.29	**5.62**	3.88
6	1	6Mhz	4cm	Large	2.13	0.68	2.62	1.55	**3.68**	1.84
				Medium	4.55	1.74	4.46	1.65	**5.72**	3.39
				Small	5.43	2.71	5.23	4.17	4.75	**5.52**
6	2	6Mhz	4cm	Large	3.49	0.78	2.81	2.13	**4.65**	1.65
				Medium	4.84	1.36	4.84	1.84	**6.30**	2.23
				Small	5.81	3.49	5.23	4.17	**6.69**	4.65
6	3	6Mhz	4cm	Large	2.91	0.78	3.20	1.45	**3.78**	1.74
				Medium	4.26	1.26	4.07	2.42	**5.72**	2.71
				Small	**6.20**	3.10	5.91	4.75	6.10	5.04
7	1	10Mhz	4cm	Large	2.62	0.58	3.59	0.78	**4.36**	1.94
				Medium	3.88	1.84	4.36	1.55	**5.04**	2.91
				Small	5.04	3.10	5.62	4.46	**6.10**	5.04
7	2	10Mhz	4cm	Large	3.20	0.87	3.49	1.45	**3.88**	1.07
				Medium	4.55	1.84	4.07	1.45	**5.33**	2.42
				Small	5.43	3.00	5.43	4.26	**6.59**	3.88
7	3	10Mhz	4cm	Large	2.62	0.78	3.00	0.87	**4.46**	2.33
				Medium	3.49	1.45	5.04	1.55	**5.62**	2.13
				Small	3.88	2.91	**5.91**	4.75	5.72	5.14
8	1	6Mhz	5cm	Large	2.23	0.68	2.52	0.78	**3.97**	3.00
				Medium	3.00	1.36	3.59	2.42	**5.72**	3.39
				Small	4.94	2.33	4.84	5.14	**6.10**	4.17
8	2	6Mhz	5cm	Large	2.13	0.68	2.71	1.16	**4.65**	1.16
				Medium	3.59	0.87	4.36	2.52	**5.43**	3.59
				Small	5.72	3.20	5.33	5.04	**6.20**	3.78
8	3	6Mhz	5cm	Large	2.81	0.48	3.29	1.74	**3.97**	0.97
				Medium	3.29	1.36	3.97	2.33	**5.81**	2.81
				Small	4.36	3.10	5.72	4.75	**6.01**	3.29
9	1	10Mhz	5cm	Large	1.45	0.48	2.23	0.78	**2.52**	0.78
				Medium	2.03	0.97	2.91	0.78	**3.29**	1.84
				Small	3.39	2.71	5.33	4.55	**6.59**	4.84
9	2	10Mhz	5cm	Large	0.78	0.97	2.23	0.58	**3.29**	0.78
				Medium	3.10	1.65	3.59	1.07	**4.75**	1.36
				Small	3.49	3.00	5.14	3.20	**6.20**	3.97
9	3	10Mhz	5cm	Large	1.16	0.48	1.36	0.29	**2.62**	1.26
				Medium	2.03	0.68	2.42	1.55	**4.75**	2.13
				Small	3.78	3.20	4.75	4.36	**6.20**	4.36
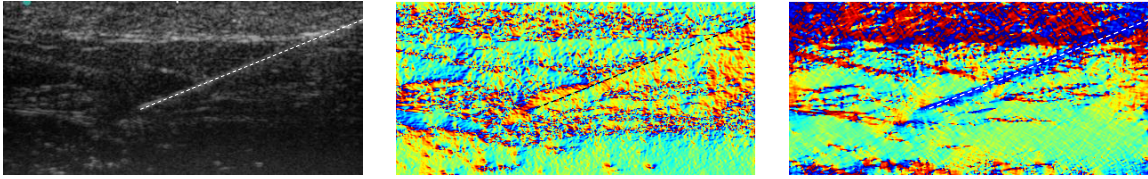
Figure 16: Ultrasound image with biopsy needle (left). Calculated local orientation for monogenic signal (middle) and 2D analytic signal (right). Center line of the needle is indicated with the dashed white and black line, respectively.

While the images give a good overview about the spatial distribution of the P-values and the boxplots nicely illustrates their statistics, it is difficult to show the results for all 81 configurations compactly. Consequently, we quantify the percentage of P-values that are above 0.85 for each image, corresponding to appropriate fits. The results are shown in tables 1 and 2. Generally, better fits are achieved for smaller window sizes. This is comprehensible, because smaller windows are more likely to contain homogeneous tissue. In the tables, we highlight the percentage of the envelope detection scheme in bold that performed best. The envelope detection with the 1D AS is best in 3.7%, the MS in 2.5%, the 2D AS in 91.4%, and 2D ASF in 2.5% of the cases. This clearly shows that the application of the 2D analytic signal leads to advantages in the statistical analysis in most of the cases. Just regarding these numbers, one is tempted to assume that 1D AS performs better than MS. This is, however, not the case because the MS outperforms the 1D AS in most of the cases that 2D AS performs best.

4. 2D Analytic Signal on B-mode Images

Next to the benefits of the 2D analytic signal for the demodulation of RF data, it also allows for a more accurate estimation of local features on B-mode images (Wietzke et al., 2009). This has the potential to increase the quality of follow-up applications such as registration (Grau et al., Sept. 2007; Mellor and Brady, 2005; Zhang et al., 2007), segmentation (Hacihaliloglu et al., 2008), and detection (Mulet-Parada and Noble, 2000), which use the local features as input. To demonstrate this, we calculate the local orientation on B-mode images showing a biopsy needle. In figure 16, we illustrate the local orientation that is estimated from the monogenic signal and the 2D analytic signal, both with filtering. The correct location of the needle is overlaid with a dashed line. The estimation from the monogenic signal shows no consistent orientation information in the region of the needle. In contrast, the improved concept of the 2D analytic signal indicates a consistent result. These images can be integrated in common algorithms for needle detection in ultrasound, such as the sticks algorithm (Czerwinski et al., 1999). Our results are in line with the findings in Wietzke et al. (2009), stating that the 2D analytic signal also leads to a more accurate estimation of i1D features in comparison to the monogenic signal.

5. Conclusion

We demonstrated that the application of the 2D analytic signal has multiple advantageous for RF and B-mode data. The demodulation of RF signals with the 2D analytic signal enables a more consistent extraction of structures, because the signal is analyzed in its natural 2D context. We further showed that the improved envelope detection enables the creation of B-mode images of enhanced quality. To validate this, we applied a proprietary post-processing filtering for ultrasound on the log-compressed images and compared the result of 1D and 2D analytic signal. Moreover, we illustrated the improved statistical properties of envelope data resulting from the 2D analytic signal by performing goodness-of-fit tests to a Nakagami distribution. This is done for multiple patients and multiple window sizes. We applied the Gamma kernel density estimation in order to be able to work with small window sizes. Finally, the advanced signal model of the 2D analytic signal leads to benefits in the estimation of local features in B-mode images, as we have illustrated for the case of needle detection.

For the demodulation, we focused on scans from a linear transducer. For curved linear transducers, the application of 2D Hilbert transforms without a previous scan conversion can be achieved with the polar Fourier transform (Averbuch et al., 2006). The integration of the bandpass filter is more challenging because of the large variation in lateral distance along the beam. This, together with the incorporation of mixture models in the statistical analysis, remains as future work.

14

$$\frac{\partial \int_{a_i}^{b_i} \Gamma\left(x \mid \alpha,\beta\right) \mathrm{d}x}{\partial \beta} = -(\alpha^2 \Gamma\left(\alpha\right))^{-1} \left[-(a_i\beta)^{\alpha} {}_2\mathrm{F}_2(\alpha,\alpha;\ 1+\alpha,1+\alpha;\ -a_i\beta) + (b_i\beta)^{\alpha} {}_2\mathrm{F}_2(\alpha,\alpha;\ 1+\alpha,1+\alpha;\ -b_i\beta) \right. \tag{27}$$

$$\left. + \alpha^2 \Gamma\left(\alpha,b_i\beta\right) \ln\left(b_i\beta\right) - \alpha^2 \Gamma\left(\alpha\right) \ln\left(b_i\beta\right) - \alpha^2 \Gamma\left(\alpha,a_i\beta\right) \ln\left(a_i\beta\right) + \alpha^2 \Gamma\left(\alpha\right) \ln(a_i\beta) - \alpha^2 \Gamma(\alpha,b_i\beta)\Psi(\alpha) + \alpha^2 \Gamma(\alpha,a_i\beta)\Psi(\alpha) \right].$$

6. Acknowledgement

Appendix A. Derivative of Nakgami Distribution

Making use of the Nakagami-Gamma relationship

$$Y \sim \mathcal{N}(x \mid \mu,\omega) \quad \Rightarrow \quad Y^2 \sim \Gamma(x \mid \mu, \frac{\omega}{\mu}), \tag{A.1}$$

the data can be transformed to follow the Gamma distribution. Hence, the required derivations of the derivatives w.r.t. to the parameters can be performed on the Gamma distribution.

Most previous approaches that perform GOF tests on ultrasound data restrict their analysis to the simpler case of Gaussian distributions (Lin et al., 2005). The Gamma distribution is

$$\Gamma(x \mid \alpha,\beta) = \frac{\beta^{\alpha} x^{\alpha-1} \mathrm{e}^{-x\beta}}{\Gamma(\alpha)}. \tag{A.2}$$

For the calculation of the of the Rao-Robson statistics (cf. equation 21), the partial derivative of the binned distribution in the interval $[a_i, b_i]$ with respect to both parameters $\{\alpha,\beta\}$ is required. The derivation with respect to the first parameter α is

$$\frac{\partial \int_{a_i}^{b_i} \Gamma\left(x \mid \alpha,\beta\right) \mathrm{d}x}{\partial \alpha} = \frac{(b_i\beta)^{\alpha} \mathrm{e}^{-b_i\beta} - (a_i\beta)^{\alpha} \mathrm{e}^{-a_i\beta}}{\beta\,\Gamma(\alpha)}. \tag{A.3}$$

Denoting the generalized hypergeometric function by ${}_2\mathrm{F}_2$, we obtain equation (27) for the derivation with respect to β.

References

Abdi, A., Kaveh, M., 2000. Performance comparison of three different estimators for the nakagami m parameter using monte carlo simulation. Communications Letters, IEEE 4, 119 –121.

Ali, R., Gooding, M., Christlieb, M., Brady, M., 2008. Advanced phase-based segmentation of multiple cells from brightfield microscopy images, in: ISBI, pp. 181–184.

Averbuch, A., Coifman, R., Donoho, D., Elad, M., Israeli, M., 2006. Fast and accurate polar Fourier transform. Applied and Computational Harmonic Analysis 21, 145–167.

Bock, R.K., Krischer, W., 1998. The Data Analysis Briefbook. Springer-Verlag New York, Inc., Secaucus, NJ, USA. 1st edition.

Boukerroui, D., Noble, J., Brady, M., 2004. On the Choice of Band-Pass Quadrature Filters. Journal of Mathematical Imaging and Vision 21, 53–80.

Carneiro, G., Jepson, A.D., 2002. Phase-based local features, in: ECCV '02: Proceedings of the 7th European Conference on Computer Vision-Part I, Springer-Verlag, London, UK. pp. 282–296.

Chen, S., 2000. Probability density function estimation using gamma kernels. Annals of the Institute of Statistical Mathematics 52, 471–480.

Cincotti, G., Loi, G., Pappalardo, M., 2001. Frequency decomposition and compounding of ultrasound medical images with wavelet packets. IEEE transactions on medical imaging 20, 764–771.

Cobbold, R., 2007. Foundations of biomedical ultrasound. Oxford University Press, USA.

Czerwinski, R., Jones, D., O'Brien, W.D., J., 1999. Detection of lines and boundaries in speckle images-application to medical ultrasound. Medical Imaging, IEEE Transactions on 18, 126 –136.

D'Agostino, R., Stephens, M., 1986. Goodness-of-fit techniques. Marcel Dekker, Inc. New York, NY, USA , 560.

Destrempes, F., Cloutier, G., 2010. A Critical Review and Uniformized Representation of Statistical Distributions Modeling the Ultrasound Echo Envelope. Ultrasound in medicine & biology 36, 1037–1051.

Destrempes, F., Meunier, J., Giroux, M.F., Soulez, G., Cloutier, G., 2009. Segmentation in ultrasonic b-mode images of healthy carotid arteries using mixtures of nakagami distributions and stochastic optimization. IEEE Trans Med Imaging 28, 215–229.

Dutt, V., 1995. Statistical analysis of ultrasound echo envelope. PhD Thesis, Mayo Graduate School.

Dutt, V., Greenleaf, J.F., 1994. Ultrasound echo envelope analysis using a homodyned k-distribution signal model. Ultrason. Imag. 16, 265–287.

Eltoft, T., 2003. Speckle: Modeling and filtering, in: Norwegian Signal Process. Symp.

Estepar, R., Washko, G., Silverman, E., Reilly, J., Kikinis, R., Westin, C., 2006. Accurate airway wall estimation using phase congruency. MICCAI .

Felsberg, M., Sommer, G., 2001. The monogenic signal. IEEE Transactions on Signal Processing 49, 3136–3144.

Felsberg, M., Sommer, G., 2004. The monogenic scale-space: A unifying approach to phase-based image processing in scale-space. Journal of Mathematical Imaging and vision 21, 5–26.

Fleet, D., Jepson, A., Jenkin, M., 1991. Phase-based disparity measurement. CVGIP: Image Understanding 53, 198–210.

Goodman, J., 2006. Speckle phenomena in optics: theory and applications. Roberts & Co.

Granlund, G.H., Knutsson, H., 1995. Signal Processing for Computer

Vision. Kluwer Academic Publishers.

Grau, V., Becher, H., Noble, J., Sept. 2007. Registration of multi-view real-time 3-d echocardiographic sequences. Medical Imaging, IEEE Transactions on 26, 1154–1165.

Hacihaliloglu, I., Abugharbieh, R., Hodgson, A., Rohling, R., 2008. Bone segmentation and fracture detection in ultrasound using 3d local phase features, in: International Conference on Medical Image Computing and Computer-Assisted Intervention (MICCAI), pp. 287–295.

Hedrick, W.R., Hykes, D.L., Starchman, D.E., 2004. Ultrasound Physics and Instrumentation. Mosby, 4 edition.

Jakeman, E., Pusey, P.N., 1976. A model for non-rayleigh sea echo. IEEE Trans. Antennas Propag. 24, 806–814.

Jensen, J., 1999. A new calculation procedure for spatial impulse responses in ultrasound. The Journal of the Acoustical Society of America 105, 3266.

Kotropoulos, C., Magnisalis, X., Pitas, I., Strintzis, M., 1994. Nonlinear ultrasonic image processing based on signal-adaptivefilters and self-organizing neural networks. Image Processing, IEEE Transactions on 3, 65–77.

Kovesi, P., 1999. Image features from phase congruency. Videre: Journal of Computer Vision Research 1.

Kovesi, P., 2008. Log-gabor filters. http://www.csse.uwa.edu.au/~pk/research/matlabfns/PhaseCongruency/Docs/convexpl.html.

Larrue, A., Noble, J., 2011. Nakagami imaging with small windows, in: Biomedical Imaging: From Nano to Macro, 2011 IEEE International Symposium on, IEEE. pp. 887–890.

Lin, N., Yu, W., Duncan, J., 2005. Left ventricular boundary segmentation from echocardiography. Medical Imaging Systems Technology 3, 89.

Lord, R.D., 1954. The use of the hankel transform in statistics. i. Pattern Recogn. Lett. 41.

Mellor, M., Brady, M., 2005. Phase mutual information as a similarity measure for registration. Medical Image Analysis 9, 330–343.

Mulet-Parada, M., Noble, J., 2000. 2D+ T acoustic boundary detection in echocardiography. Medical Image Analysis 4, 21–30.

Myronenko, A., Song, X., Sahn, D., 2009. Maximum Likelihood Motion Estimation in 3D Echocardiography through Non-rigid Registration in Spherical Coordinates. Functional Imaging and Modeling of the Heart , 427–436.

Nakagami, N., 1960. The m-distribution, a general formula for intensity distribution of rapid fadings, in: Hoffman, W.G. (Ed.), Statistical Methods in Radio Wave Propagation. Oxford, England: Pergamon.

Noble, J., 2010. Ultrasound image segmentation and tissue characterization. Proceedings of the Institution of Mechanical Engineers, Part H: Journal of Engineering in Medicine 224, 307.

Shankar, P., 1995. A model for ultrasonic scattering from tissues based on the k distribution. Physics in medicine and biology 40, 1633.

Shankar, P., Dumane, V., Reid, J., Genis, V., Forsberg, F., Piccoli, C., Goldberg, B., 2001. Classification of ultrasonic B-mode images of breast masses using Nakagami distribution. Ultrasonics, Ferroelectrics and Frequency Control, IEEE Transactions on 48, 569–580.

Shankar, P., Dumane, V., Reid, J., Genis, V., Forsberg, F., Piccoli, C., Goldberg, B., 2002. Classification of ultrasonic b-mode images of breast masses using nakagami distribution. Ultrasonics, Ferroelectrics and Frequency Control, IEEE Transactions on 48, 569–580.

Shankar, P.M., Reid, J.M., Ortega, H., Piccoli, C.W., Goldberg, B.B., 1993. Use of non-rayleigh statistics for the identification of tumors in ultrasonic b-scans of the breast. IEEE Trans. Med. Imag. 12, 687–692.

Szilágyi, T., Brady, S.M., 2009. Feature extraction from cancer images using local phase congruency: a reliable source of image descriptors, in: ISBI'09: Proceedings of the Sixth IEEE international conference on Symposium on Biomedical Imaging, IEEE Press, Piscataway, NJ, USA. pp. 1219–1222.

Tao, Z., Tagare, H., Beaty, J., 2006. Evaluation of four probability distribution models for speckle in clinical cardiac ultrasound images. Medical Imaging, IEEE Transactions on 25, 1483–1491.

Wachinger, C., Klein, T., Navab, N., 2011. The 2D Analytic Signal on RF and B-mode Ultrasound Images, in: Information Processing in Medical Imaging (IPMI).

Wachinger, C., Klein, T., Navab, N., 2012. Locally adaptive nakagami-based ultrasound similarity measures. Ultrasonics 52, 547 – 554.

Wang, P., Kelly, C., Brady, M., 2009. Application of 3d local phase theory in vessel segmentation, in: ISBI'09: Proceedings of the Sixth IEEE international conference on Symposium on Biomedical Imaging, IEEE Press, Piscataway, NJ, USA. pp. 1174–1177.

Wietzke, L., Sommer, G., Fleischmann, O., 2009. The geometry of 2d image signals, in: CVPR, pp. 1690–1697.

Xiaoxun, Z., Yunde, J., 2006. Local Steerable Phase (LSP) Feature for Face Representation and Recognition, in: Conference on Computer Vision and Pattern Recognition.

Zagzebski, J., 1996. Essentials Of Ultrasound Physics. Mosby, 1 edition.

Zang, D., Wietzke, L., Schmaltz, C., Sommer, G., 2007. Dense optical flow estimation from the monogenic curvature tensor. Scale Space and Variational Methods in Computer Vision , 239–250.

Zetsche, C., Barth, E., 1990. Fundamental limits of linear filters in the visual processing of two dimensional signals. Vision Research 30.

Zhang, W., Noble, J.A., Brady, J.M., 2007. Spatio-temporal registration of real time 3d ultrasound to cardiovascular mr sequences, in: MICCAI, pp. 343–350.

16